Search for direct production of electroweakinos in final states with one lepton, missing transverse momentum and a Higgs boson decaying into two b-jets in pp collisions at $\sqrt{s}$ = 13 TeV with the ATLAS detector

The ATLAS Collaboration

The results of a search for electroweakino pair production $pp \rightarrow \tilde{\chi}_1^\pm \tilde{\chi}_2^0$ in which the chargino ($\tilde{\chi}_1^\pm$) decays into a W boson and the lightest neutralino ($\tilde{\chi}_1^0$), while the heavier neutralino ($\tilde{\chi}_2^0$) decays into the Standard Model 125 GeV Higgs boson and a second $\tilde{\chi}_1^0$ are presented. The signal selection requires a pair of b-tagged jets consistent with those from a Higgs boson decay, either an electron or muon from the W boson decay, together with missing transverse momentum from the corresponding neutrino and the stable neutralinos. The analysis is based on data corresponding to 139 fb^{-1} of $\sqrt{s}$ = 13 TeV pp collisions provided by the Large Hadron Collider and recorded by the ATLAS detector. No statistically-significant evidence is found for an excess of events above the Standard Model expectation. Limits are set on the direct production of the electroweakinos in simplified models, assuming pure wino cross sections. Masses of $\tilde{\chi}_1^\pm / \tilde{\chi}_2^0$ up to 740 GeV are excluded at 95% confidence-level for a massless $\tilde{\chi}_1^0$.

1 Introduction

The Standard Model (SM) is a remarkably successful theory, yet it is clear that this theory is not complete when describing nature. The discovery in 2012 of the SM Higgs boson [1–4], by the ATLAS and CMS collaborations, confirmed the importance of the electroweak symmetry breaking mechanism and the hierarchy problem [5–8]. Supersymmetry (SUSY) [9–14], a theoretical extension to the SM, elegantly resolves the hierarchy problem by introducing a new fermion (boson) supersymmetric partner for each boson (fermion) in the SM. In SUSY models which conserve R-parity [15], the SUSY particles are produced in pairs. Furthermore, the lightest supersymmetric particle (LSP) is stable and weakly interacting, thus constituting a viable dark matter candidate [16, 17].

In SUSY scenarios the partners of the SM Higgs boson and the gauge bosons, known as higgsinos, winos (partners of the $SU(2)_L$ gauge fields), and bino (partner of the $U(1)$ gauge field) are collectively referred as electroweakinos. Charginos $\tilde{\chi}_i^\pm$ ($i = 1, 2$) and neutralinos $\tilde{\chi}_j^0$ ($j = 1, 2, 3, 4$) are the electroweakino mass eigenstates which are linear superpositions of higgsinos, winos, and bino. For the models considered in this paper, the lightest neutralino ($\tilde{\chi}_1^0$) is a bino-like LSP. The lightest chargino ($\tilde{\chi}_1^\pm$) and next-to-lightest neutralino ($\tilde{\chi}_2^0$) are wino-like and nearly mass degenerate.

Naturalness considerations [18, 19] suggest that the lightest of the electroweakinos have masses near the electroweak scale. In scenarios where the strongly produced SUSY particles are heavier than a few TeV, the direct production of electroweakinos may be the dominant SUSY production mechanism at the Large Hadron Collider (LHC). The lightest chargino and next-to-lightest neutralino can decay via $\tilde{\chi}_1^\pm \to W \tilde{\chi}_1^0$ and $\tilde{\chi}_2^0 \to h/Z \tilde{\chi}_1^0$ respectively [20–22] in scenarios where the lepton superpartners are heavier than the electroweakinos. In this case the decay via the Higgs boson is dominant for many choices of SUSY parameters, as long as $m(\tilde{\chi}_2^0) - m(\tilde{\chi}_1^0) > m(h)$. Scenarios with light electroweakinos also provide a possible explanation for the discrepancy observed in the muon anomalous magnetic moment $g - 2$ measurement with respect to the SM predictions [23–25].

This paper presents a search for direct production of electroweakinos in pp collisions produced at the LHC at $\sqrt{s} = 13$ TeV. This analysis is designed to be sensitive to direct production of a chargino and a neutralino that promptly decay as $\tilde{\chi}_1^\pm \to W \tilde{\chi}_1^0$ and $\tilde{\chi}_2^0 \to h \tilde{\chi}_1^0$. The search targets the W boson decaying into an electron or muon (and corresponding neutrino) and the Higgs boson into a pair of b-quarks, as shown in Figure 1. The signature consists of exactly one light lepton (e or μ), two jets originating from the fragmentation of b-quarks, and missing transverse momentum (p_T^{miss}) from neutralinos and neutrinos. A set of simplified SUSY models is used to optimise the search and interpret the results. The branching ratios of $\tilde{\chi}_1^\pm \to W \tilde{\chi}_1^0$ and $\tilde{\chi}_2^0 \to h \tilde{\chi}_1^0$ are assumed to be 100%. The branching ratio of $h \to b\bar{b}$ is considered to be 58.3% as expected for the SM Higgs boson.

Previous searches for charginos and neutralinos at the LHC targeting decays via the Higgs boson have been reported by the ATLAS [26, 27] and CMS [28] collaborations. The search presented here significantly extends the sensitivity to the SUSY parameter space due in part to the increased luminosity and an improved two-dimensional fit procedure with respect to the last ATLAS published search in the same final state.
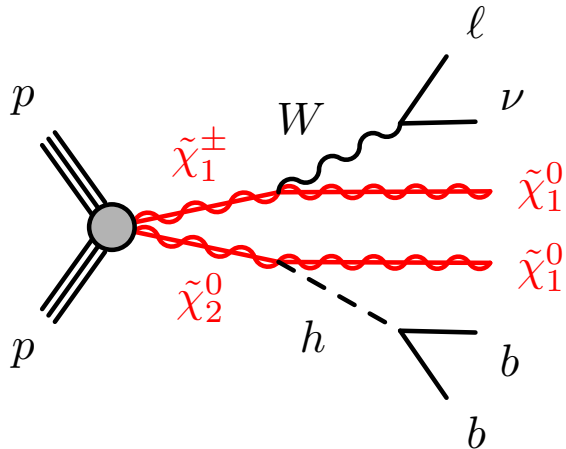
Figure 1: A diagram illustrating the signal scenario considered for the production of a chargino and a next-to-lightest neutralino.

2 ATLAS detector

The ATLAS detector [29] is a multipurpose particle detector with a nearly 4π coverage in solid angle.[1]

It consists of an inner tracking detector surrounded by a thin superconducting solenoid providing a 2 T axial magnetic field, electromagnetic and hadron calorimeters, and a muon spectrometer. The inner tracking detector covers the pseudorapidity range $|\eta| < 2.5$. It consists of silicon pixel, silicon microstrip, and transition radiation tracking detectors. A new inner pixel layer, the insertable B-layer [30, 31], was added at a mean radius of 3.3 cm during the period between Run 1 and Run 2 of the LHC improving the identification of b-jets. Lead/liquid-argon (LAr) sampling calorimeters provide electromagnetic (EM) energy measurements with high granularity. A hadron (steel/scintillator-tile) calorimeter covers the central pseudorapidity range ($|\eta| < 1.7$). The end-cap and forward regions are instrumented with LAr calorimeters for both EM and hadronic energy measurements up to $|\eta| = 4.9$. The muon spectrometer surrounds the calorimeters and is based on three large air-core toroidal superconducting magnets with eight coils each. The field integral of the toroids ranges between 2.0 and 6.0 T · m across most of the detector. The muon spectrometer includes a system of precision tracking chambers and fast detectors for triggering. A two-level trigger system is used to select events. The first-level trigger is implemented in hardware and uses a subset of the detector information to reduce the accepted rate to at most nearly 100 kHz. This is followed by a software-based trigger that reduces the accepted event rate to 1 kHz on average depending on the data-taking conditions.

---

[1] ATLAS uses a right-handed coordinate system with its origin at the nominal interaction point in the center of the detector. The positive x-axis is defined by the direction from the interaction point to the center of the LHC ring, with the positive y-axis pointing upwards, while the beam direction defines the z-axis. Cylindrical coordinates (r, ϕ) are used in the transverse plane, ϕ being the azimuthal angle around the z-axis. The pseudorapidity η is defined in terms of the polar angle θ by $\eta = -\ln\tan(\theta/2)$. Rapidity is defined as $y = 0.5\ln[(E + p_z)/(E - p_z)]$ where E denotes the energy and p_z is the component of the momentum along the beam direction. The angular distance ΔR is defined as $\sqrt{(\Delta y)^2 + (\Delta \phi)^2}$.

3 Dataset and simulated events

The results are obtained using 139 fb^{-1} of pp LHC collision data collected between 2015 and 2018 by the ATLAS detector, with a center-of-mass energy of 13 TeV and a 25 ns proton bunch crossing interval. In 2015-2016 the average number of interactions per bunch crossing (pile-up) was $\langle\mu\rangle = 20$ increasing to $\langle\mu\rangle = 38$ in 2017 and to $\langle\mu\rangle = 37$ in 2018. The uncertainty in the combined 2015-2018 integrated luminosity is 1.7%. It is derived from the calibration of the luminosity scale using x-y beam separation scans, following a methodology similar to that detailed in Ref. [32], and using the LUCID-2 detector for the baseline luminosity measurements [33].

Monte Carlo (MC) simulated datasets are used to model the SM backgrounds and evaluate signal selection efficiency and yields. All simulated samples were produced using the ATLAS simulation infrastructure [34] and GEANT4 [35], or a faster simulation based on a parametrisation of the calorimeter response and GEANT4 for the other detector systems. All simulated events were generated with a varying number of minimum-bias interactions overlaid on the hard-scattering event to model the multiple proton-proton interactions in the same and nearby bunch crossings. The simulated events were reconstructed with the same algorithms as those used for data.

The backgrounds considered in this analysis are: $t\bar{t}$ pair production; single-top production ($s-$channel, $t-$channel, and associated Wt production); W/Z+jets production; $t\bar{t}$ production with an electroweak boson (ttV); Higgs boson production (tth, Vh); diboson (WW, WZ, ZZ) and triboson (VVV where $V = W, Z$) production. Background samples were simulated using different MC event generators depending on the process. All background processes are normalised to the best available theoretical calculation of their respective cross-sections. The SHERPA samples used for W+jets modeling include up to 4 partons at leading order in the matrix element. The production of jets containing heavy flavor hadrons is dominated by events with heavy quarks in these matrix element partons. The event generators, the parton shower and hadronisation routine, the underlying-event parameter tunes, and the parton distribution function (PDF) sets used in simulating the SM background processes, along with the accuracy of theoretical cross-sections are summarized in Table 1.

For all samples showered with PYTHIA, the EvtGen v1.2.0 [36] program was used to simulate the properties of the bottom- and charm-hadron decays. Several samples produced without detector simulation are employed to estimate systematic uncertainties associated with the specific configuration of the MC generators used for the nominal SM background samples. They include variations of the renormalisation and factorisation scales, the CKKW-L [37] matching scale, as well as different PDF sets and fragmentation/hadronisation models. Details of the MC modelling uncertainties are discussed in Section 7.

The SUSY signal samples have been generated using MADGRAPH5_aMC@NLO v2.6.2 [38] and PYTHIA v8.230 [39] with the A14 [40] set of tuned parameters for the modelling of the parton showering (PS), hadronisation and underlying event. The matrix element (ME) calculation was performed at tree level and includes the emission of up to two additional partons. The ME–PS matching was done using the CKKW-L prescription, with a matching scale set to one quarter of the chargino and next-to-lightest neutralino mass. The NNPDF2.3LO [41] PDF set was used.

Signal cross sections are calculated at next-to-leading-order (NLO) accuracy in the strong coupling constant, adding the resummation of soft gluon emission at next-to-leading-logarithm accuracy (NLO+NLL) [42–44]. The nominal cross-section and its uncertainty are taken as the midpoint and half-width of an envelope of cross-section predictions using different PDF sets and factorisation and renormalisation scales, as described in Ref. [45]. The simplified model has two parameters, the first being the mass of the $\tilde{\chi}_1^\pm$ and $\tilde{\chi}_2^0$ (which

Table 1: Overview of MC generators used for different simulated event samples.

Process	Generator	PS and hadronisation	Tune	PDF	Cross-section
$t\bar{t}$	Powheg-Box v2 [46, 47]	Pythia v8.230 [39]	A14 [40]	NNPDF2.3LO [41]	NNLO+NNLL [48]
Single top	Powheg-Box v2	Pythia v8.230	A14	NNPDF2.3LO	NLO+NNLL [49]
W/Z+jets	SHERPA v2.2.1[50]	SHERPA v2.2.1	Sherpa standard	NNPDF3.0NNLO	NNLO [51]
Diboson	SHERPA v2.2.1 & v2.2.2	SHERPA v2.2.1 & v2.2.2	Sherpa standard	NNPDF3.0NNLO	NLO
Triboson	SHERPA v2.2.1 & v2.2.2	SHERPA v2.2.1 & v2.2.2	Sherpa standard	NNPDF3.0NNLO	NLO
$t\bar{t} + V$	MadGraph5_aMC@NLO v2.3.3	Pythia v8.210	A14	NNPDF2.3LO	NLO [52]
tth	Powheg-Box v2	Pythia v8.230	AZNLO [53]	CTEQ6L1 [54]	NLO [55]
Vh	Powheg-Box v2	Pythia v8.212	A14	NNPDF2.3LO	NLO [55]

are assumed to be equal), and the second being the mass of the $\tilde{\chi}_1^0$. The signal cross sections decrease as the $\tilde{\chi}_1^\pm/\tilde{\chi}_2^0$ mass increases, ranging from 769 fb for a 250 GeV $\tilde{\chi}_1^\pm/\tilde{\chi}_2^0$ mass to 1.3 fb for a 1000 GeV $\tilde{\chi}_1^\pm/\tilde{\chi}_2^0$ mass.

4 Event reconstruction

Events are required to have at least one reconstructed proton-proton interaction vertex with a minimum of two associated tracks each having $p_T > 500$ MeV. In events with multiple vertices, the one with the highest sum of squared transverse momenta of associated tracks is chosen as the primary vertex (PV) [56]. A set of baseline quality criteria are applied to reject events with non-collision backgrounds or detector noise [57].

Two identification levels are defined for leptons and jets: "Baseline" and "Signal". "Baseline" leptons and jets are selected with looser identification criteria, and are used in the E_T^{miss} computation as well as in resolving possible reconstruction ambiguities. "Signal" leptons and jets are a subset of the baseline objects with tighter quality requirements which are used to define the search regions. Isolation criteria, defined with a list of tracking-based and calorimeter-based variables, are used to discriminate signal leptons against semileptonic heavy-flavour decays and jets misidentified as leptons.

Electron candidates are reconstructed from energy deposits in the electromagnetic calorimeter that are matched to charged particle tracks in the inner detector [58]. Baseline electrons are required to satisfy $p_T > 7$ GeV and $|\eta| < 2.47$. They are identified using the "loose" operating point provided by a likelihood-based algorithm, a multivariate analysis technique evaluating multiple features (such as calorimeter-based shower shapes, inner-detector track and impact parameters) to make a selection decision [59]. The number of hits in the innermost pixel layer is used for discriminating between electrons and converted photons. The longitudinal impact parameter z_0 relative to the PV is required to satisfy $|z_0 \sin\theta| < 0.5$ mm. To increase background rejection, the "tight" likelihood operating point is applied for signal electron identification and the significance of the transverse impact parameter d_0 must satisfy $|d_0/\sigma(d_0)| < 5$. Signal electrons with $p_T < 200$ GeV are further refined using the *FCLoose* isolation working point, while those with larger p_T are required to pass the *FCHighPtCaloOnly* isolation working point, as described in Ref. [58].

Muon candidates are reconstructed from matching tracks in the ID and MS, refined through a global fit which uses the hits from both subdetectors [60]. Baseline muons must have $p_T > 6$ GeV, $|\eta| < 2.7$ and satisfy the "medium" identification criteria. Similar to electrons, the longitudinal impact parameter z_0 relative to the PV is required to satisfy $|z_0 \sin\theta| < 0.5$ mm. Signal muons are further defined with tighter η

and impact parameter requirements, $|\eta| < 2.5$ and $|d_0/\sigma(d_0)| < 3$. The *FCLoose* isolation working point is also required for signal muons [60].

Jets are reconstructed from three-dimensional topological energy clusters in the calorimeters using the anti-k_t algorithm with a radius parameter $R = 0.4$ [61]. Baseline jets are selected in the region $|\eta| < 4.5$ with $p_T > 20$ GeV. To suppress hard-scatter jets from pile-up, the jets with $|\eta| < 2.8$ and $p_T < 120$ GeV are required to satisfy the "medium" working point of the Jet Vertex Tagger (JVT), a tagging algorithm that identifies jets originating from the PV using track information [62]. The selection of signal jets is further refined by requiring them to be in $|\eta| < 2.8$ and have $p_T > 30$ GeV.

Jets containing b-hadrons, referred to as b-tagged jets, are identified using the MV2c10 algorithm, a multivariate discriminant based on the track impact parameters and displaced secondary vertices [63]. These b-tagged jets are reconstructed in the region $|\eta| < 2.5$ with $p_T > 20$ GeV. The b-tagging working point provides a consistent efficiency of 77% for simulated $t\bar{t}$ events, with a rejection rate of 6 and 134 for jets containing c-hadrons and light-flavour jets, respectively [64].

To resolve the reconstruction ambiguities between electrons, muons and jets, an overlap removal procedure is applied to baseline objects. First, any electron sharing the same ID track with a muon is rejected. If it shares the same ID track with another electron, the one with lower p_T is discarded. Next, jets are rejected if they lie within $\Delta R = 0.2$ of a muon or if the muon is matched to the jet through ghost association [65]. Subsequently, electrons within a cone with radius $\Delta R = \min(0.4, 0.04 + 10 \text{ GeV}/p_T)$ from a jet are removed. Last, muons within a cone, defined in the same way as for electrons, from the remaining jet are removed.

The missing transverse momentum, $\boldsymbol{p}_T^{\text{miss}}$, and its magnitude, E_T^{miss}, are calculated using the negative vectorial sum of the transverse momentum of all reconstructed objects (electrons, muons, jets and photons [66]) and the soft term. The soft term is reconstructed from all tracks associated with the PV but not associated to any reconstructed physics objects. Tracks not associated with the PV are not considered in the E_T^{miss} calculation, improving the E_T^{miss} resolution by suppressing the effect of pile-up [67, 68].

Corrections are applied to simulated events to account for the trigger, identification and reconstruction efficiency differences between data and simulation.

5 Event selection

Events are recorded with the lowest threshold E_T^{miss} trigger available, which is fully efficient for selecting events when the offline requirement of $E_T^{\text{miss}} > 240$ GeV is applied. To target the signal events, which have a leptonically-decaying W and a Higgs boson decaying via a $b\bar{b}$ pair, events are required to have exactly one signal electron or muon (but not both) and either two or three signal jets, precisely two of which must be b-tagged. The signal regions (SR) are defined using variables which suppress background contributions and increase the sensitivity for signal. These variables are based on the kinematic properties of the b-jets, the lepton and the missing transverse momentum, and are defined as follows:

- the invariant mass of the two b-jets, $m_{b\bar{b}}$, is required to be in the range $100 < m_{b\bar{b}} < 140$ GeV, in order to preferentially select b-jets from the Higgs boson decays;

- the invariant mass of the lepton and the leading b-jet, $m(\ell, b_1)$. For $t\bar{t}$ or single-top (in particular in Wt-channel) backgrounds, if the lepton and the leading b-jet originate from the same top-quark, $m(\ell, b_1)$ distribution has an endpoint at $\sqrt{m^2(t) - m^2(W)}$. For signal events, the lepton and b-jet are

produced from the $\tilde{\chi}_1^\pm$ and $\tilde{\chi}_2^0$ decay chains, respectively. The distribution of the invariant mass depends on the mass of the SUSY particles. For signal events with high mass $\tilde{\chi}_1^\pm/\tilde{\chi}_2^0$, this observable provides good discrimination against background events;

- the transverse mass, m_T, is defined from the lepton transverse momentum $\boldsymbol{p}_T^\ell$ and $\boldsymbol{p}_T^{\mathrm{miss}}$ as

$$m_T = \sqrt{2 p_T^\ell E_T^{\mathrm{miss}} (1 - \cos[\Delta\phi(\boldsymbol{p}_T^\ell, \boldsymbol{p}_T^{\mathrm{miss}})])},$$

where $\Delta\phi(\boldsymbol{p}_T^\ell, \boldsymbol{p}_T^{\mathrm{miss}})$ is the azimuthal angle between $\boldsymbol{p}_T^\ell$ and $\boldsymbol{p}_T^{\mathrm{miss}}$. For W+jets and semileptonic $t\bar{t}$ events, in which one on-shell W boson decays leptonically, the observable has an upper endpoint at the W-boson mass. The m_T distribution for signal events extends significantly above m_W;

- the contransverse mass [69, 70] of two b-jets, m_{CT}, is defined as:

$$m_{\mathrm{CT}} = \sqrt{2 p_T^{b_1} p_T^{b_2} (1 + \cos\Delta\phi_{bb})},$$

where $p_T^{b_1}$ and $p_T^{b_2}$ are the transverse momenta of the two leading b-jets and $\Delta\phi_{bb}$ is the azimuthal angle between them. For the $t\bar{t}$ background, the observable has an upper endpoint at $(m^2(t) - m^2(W))/m(t)$. A requirement that m_{CT} be larger than 180 GeV efficiently suppresses the $t\bar{t}$ background.

An overview of the signal region definitions can be found in Table 2. Three separate classes of signal regions are defined, progressively targeting increasing mass differences between the $\tilde{\chi}_1^\pm$ (and its almost degenerate $\tilde{\chi}_2^0$ wino partner) and the $\tilde{\chi}_1^0$. These regions are denoted SR-LM, SR-MM and SR-HM indicating low (LM), medium (MM) and high (HM) mass differences respectively. Requirements on m_T make the three regions mutually exclusive. Of the three signal regions, SR-LM selects the smallest values of m_T. It targets signal models with a mass-splitting between the $\tilde{\chi}_2^0$ (and hence the $\tilde{\chi}_1^\pm$) and the $\tilde{\chi}_1^0$ that is similar to the Higgs boson mass. The other two signal regions select progressively larger mass differences by requiring larger values of m_T. The signal region with the highest requirement on m_T, SR-HM, also requires $m(\ell, b_1) > 120$ GeV in order to further suppress backgrounds containing top quarks. The three signal regions otherwise share a common set of selections on E_T^{miss}, $m_{b\bar{b}}$ and m_{CT}.

When setting model-dependent exclusion limits ("excl."), each of the three SRs is further binned in m_{CT} and a simultaneous fit is performed across the three SRs, comprising nine bins in total and forming a two-dimensional fit. The multi-bin approach enhances the sensitivity to a range of SUSY scenarios with different properties. For model-independent limits and null-hypothesis tests ("disc." for discovery), the various m_{CT} bins are merged for each of the three SRs. Furthermore the upper bound on m_T is removed for SR-LM and SR-MM. The fit strategy is detailed in Section 6. The systematic uncertainties, fit and interpretation results discussed in the following sections are based on the exclusion SRs, while the model-independent results are based on the discovery SRs.

6 Background estimation

The expected backgrounds in each signal region are determined in a profile likelihood fit, called a "background-only fit". In this fit, the normalisation of the backgrounds is adjusted to match the data in control regions (CR) with negligible signal contamination. The resulting normalisation factors are then used to correct the expected yields of the corresponding backgrounds in the various signal regions. The control regions – as detailed in the following – are designed to be enriched in the major background

Table 2: Overview of the selection criteria for the signal regions. Each one of the "excl." SR is binned in three m_{CT} regions.

	SR-LM	SR-MM	SR-HM
N_{lepton}		$= 1$	
p_{T}^{ℓ} [GeV]		$> 7(6)$ for $e(\mu)$	
N_{jet}		$= 2$ or 3	
$N_{b-\mathrm{jet}}$		$= 2$	
$E_{\mathrm{T}}^{\mathrm{miss}}$ [GeV]		> 240	
$m_{b\bar{b}}$ [GeV]		$\in [100, 140]$	
$m(\ell, b_1)$ [GeV]	–	–	> 120
m_{T} [GeV](excl.)	$\in [100, 160]$	$\in [160, 240]$	> 240
m_{CT} [GeV](excl.)		$\{\in [180, 230], \in [230, 280], > 280\}$	
m_{T} [GeV](disc.)	> 100	> 160	> 240
m_{CT} [GeV](disc.)		> 180	

processes: $t\bar{t}$, single top (dominated by Wt in all considered regions) and W+jets processes. They were designed to be non-overlapping with the signal regions and also mutually exclusive. A probability density function is defined for each of the control regions. The inputs are the observed event yield and the predicted background yield from simulation with Poisson statistical uncertainties as well as with systematic uncertainties as nuisance parameters. The nuisance parameters are constrained by Gaussian distributions with widths corresponding to the sizes of the uncertainties. The systematic uncertainties are detailed in Section 7. The product of all the probability density functions forms the likelihood. Normalisation and nuisance parameters are correlated in all regions participating in the fit. The likelihood is maximized by adjusting normalisation and nuisance parameters. The extrapolation of the adjusted normalisation and nuisance parameters to the signal regions is checked in validation regions (VR), as defined below, which kinematically resemble the signal regions, but are expected to have lower signal contamination. The VRs are non-overlapping with both the CRs and SRs.

Subdominant background processes, such as Z+jets, diboson and multiboson, $t\bar{t}$ +V, $t\bar{t}$ +h and Vh, which have no dedicated control regions, are normalised to the cross-sections indicated in Table 1. In the same way as for the dominant backgrounds, their expected yields in the SRs may be subject to statistical and systematic uncertainties. Backgrounds with fake leptons such as jets mis-reconstructed as a lepton, and events with leptons originating from a jet produced by heavy-flavour quarks or from photon conversions are found to be negligible.

The $t\bar{t}$ background estimation relies on a set of three CRs, each with an m_{T} selection the same as in the SRs (TR-LM, TR-MM, TR-HM). In order to obtain samples enriched in $t\bar{t}$ events, the requirement on $m(\ell, b_1)$ are removed and the selection criteria on m_{CT} and $m_{b\bar{b}}$ are inverted with respect to the SRs. These three control region are simultaneously fit to obtain a single normalisation factor. W+jets contributions in the SRs are constrained by a single CR (WR) defined similarly to the SRs but with less stringent lower bounds on m_{T} and $m_{b\bar{b}}$. The single top CR (STR) requires the events to satisfy the SR requirements except that for this CR it is required that $m_{\mathrm{T}} > 100$ GeV and $m_{b\bar{b}} > 195$ GeV.

Two sets of VRs are defined for each SR, including the off-peak and the on-peak $m_{b\bar{b}}$ regions, with the same m_{T} as in the SR. The on-peak VRs validate the extrapolation from the CRs to the SRs in $m_{b\bar{b}}$ and the off-peak VRs in m_{CT}. A summary of all CR and VR section criteria is reported in Table 3.

Table 3: Overview of CR and VR definitions, all region share the same selection as the SR for all variables except $m(\ell, b_1)$, which is not used in CR and VR definition.

CR	TR-LM	TR-MM	TR-HM	WR	STR	
$m_{b\bar{b}}$ [GeV]	<100 or >140			∈ [50, 80]	>195	
m_T [GeV]	∈ [100, 160]	∈ [160, 240]	>240	∈ [50, 100]	>100	
m_CT [GeV]	<180			>180	>180	
VR	**VR-onLM**	**VR-onMM**	**VR-onHM**	**VR-offLM**	**VR-offMM**	**VR-offHM**
$m_{b\bar{b}}$ [GeV]	∈ [100, 140]			∈ [50, 80] ∪ [160, 195]	∈ [50, 80] ∪ [160, 195]	∈ [50, 75] ∪ [165, 195]
m_T [GeV]	∈ [100, 160]	∈ [160, 240]	>240	∈ [100, 160]	∈ [160, 240]	>240
m_CT [GeV]	<180			>180		

7 Systematic uncertainties

Systematic uncertainties are evaluated for all simulated signal and background events. For the dominant backgrounds with dedicated control regions, the systematic uncertainties impact the extrapolation from the control regions to the corresponding signal regions. For all other backgrounds estimated from simulation, the uncertainties affect the overall cross-section normalisation and the acceptance of the analysis selection. Uncertainties arising from theoretical modelling and detector effects are estimated and discussed below. A breakdown of the dominant systematic uncertainties on background estimates in the various exclusion signal regions is summarized in Table 4.

Several uncertainties in the theoretical modelling of the single top and $t\bar{t}$ backgrounds are considered. Uncertainties due to the choice of the hard scatter generation program are estimated by comparing Powheg generated events, showered using Pythia 8, with ones generated by aMC@NLO and showered with Pythia 8, while the parton shower models are evaluated by comparing Powheg generated samples showered using Pythia 8 with Powheg samples showered using Herwig 7. The uncertainties from the modelling of initial and final state radiation are assessed by varying the renormalisation and factorisation scales up and down by a factor of two, with the radiation setting varied as well. For single top Wt production, the impact of interference between single-resonant and double-resonant top-quark production is also considered by comparing the nominal sample generated using the diagram removal method to a sample generated using the diagram subtraction method [71]. For the different signal regions, the dominant uncertainty sources are the $t\bar{t}$ parton shower in SR-LM (10%), and the single top generator uncertainties in SR-MM (10%) and SR-HM (21%).

Theory uncertainties affecting the generator predictions for W/Z+jets, diboson, triboson and $t\bar{t}$ +W/Z samples are estimated by taking the envelope of the seven-point scale variations of the renormalisation and factorisation scales. For W/Z+jets, the uncertainties on the PDF variations, as well as the variations of matching and resummation scales are also considered. Additionally, an overall 6% (20%) systematic uncertainty in the inclusive cross-section is considered for diboson (triboson) sample [72]. Similar cross-section uncertainties are also assigned for other small background contributions.

Theory uncertainties on the expected yields for SUSY signals are estimated by varying by a factor of two the parameters corresponding to the factorisation, renormalisation, and CKKW-L matching scales, as well as the Pythia 8 shower tune parameters. The overall uncertainties range from about 10% in the region with a large splitting between the $\tilde{\chi}_2^0/\tilde{\chi}_1^\pm$ and $\tilde{\chi}_1^0$ masses to about 25% in the mass spectra with small mass splitting.

Table 4: Breakdown of the dominant systematic uncertainties on background estimates in the various exclusion signal regions. Note that the individual uncertainties can be correlated, and do not necessarily add up quadratically to the total background uncertainty. The percentages show the size of the uncertainty relative to the total expected background.

Signal Region	SR-LM	SR-MM	SR-HM
Total background expectation	27	8.6	8.1
Total uncertainty	±4 [15%]	±2.2 [25%]	±2.7 [34%]
Theoretical systematic uncertainties			
$t\bar{t}$	±2.6 [10%]	±0.6 [7%]	±0.33 [4%]
Single top	±0.8 [2.7%]	±1.1 [12%]	±1.9 [23%]
W+jets	±0.23 [0.9%]	±0.07 [0.8%]	±0.19 [2.3%]
Other backgrounds	±0.13 [0.5%]	±0.15 [1.7%]	±0.08 [1.0%]
MC statistical uncertainties			
MC statistics	±1.7 [6%]	±1.1 [13%]	±1.2 [14%]
Uncertainties on the background normalisation			
Normalisation of dominant backgrounds	±1.3 [5%]	±1.6 [18%]	±1.3 [16%]
Experimental systematic uncertainties			
E_T^{miss}/JVT/pile-up/trigger	±1.8 [7%]	±0.4 [4%]	±0.4 [5%]
Jet energy resolution	±1.6 [6%]	±0.5 [6%]	±0.4 [5%]
b-tagging	±1.1 [4%]	±0.29 [3.4%]	±0.13 [1.5%]
Jet energy scale	±0.9 [3.2%]	±0.9 [10%]	±0.29 [4%]
Lepton uncertainties	±0.32 [1.2%]	±0.09 [1.0%]	±0.19 [2.3%]

The dominant detector systematic effects are the uncertainties associated with the jet energy scale (JES) and jet resolution (JER), the E_T^{miss} modelling and pile-up. The jet uncertainties are measured as a function of the p_T and η of the jet, the pile-up conditions and the jet flavour composition. They are determined using a combination of data and simulation, through measurements of the jet balance in dijet, Z+jets and γ+jets events [73]. The systematic uncertainties on the E_T^{miss} modelling are derived by propagating the uncertainties on the energy and momentum scale of each of the objects entering the calculation, and the uncertainties on the soft term resolution and scale [68]. A pile-up reweighting procedure is applied to simulation to match the distribution of the number of reconstructed vertices observed in data. The corresponding uncertainty is derived by reweighting such that the $\langle\mu\rangle$ is changed by ±4%. The impact of experimental uncertainties is less significant compared to the theoretical ones in all signal regions: the largest experimental source contributes 5–10% depending on the SR. The MC statistical uncertainties contribute 5–18% depending on the SR.

Table 5: Background fit results for the exclusion SR regions. The errors shown are the statistical plus systematic uncertainties. Uncertainties on the fitted yields are symmetric by construction, except where the negative error is truncated at an event yield of zero.

SR-LM	All m_{CT} bins	low m_{CT}	med. m_{CT}	high m_{CT}
Observed	34	16	11	7
Expected	27 ± 4	8.8 ± 2.8	11.3 ± 3.1	7.3 ± 1.5
$t\bar{t}$	16.2 ± 3.4	4.4 ± 2.2	7.3 ± 2.5	4.6 ± 1.2
Single top	2.7 ± 1.8	1.3 ± 1.1	$0.9^{+1.0}_{-0.9}$	0.6 ± 0.6
W+jets	5.5 ± 2.0	2.0 ± 0.9	2.4 ± 1.3	1.1 ± 0.5
Di-/Multiboson	0.67 ± 0.19	0.39 ± 0.13	$0.09^{+0.11}_{-0.09}$	0.18 ± 0.04
Others	2.23 ± 0.29	0.81 ± 0.25	0.64 ± 0.15	0.77 ± 0.12
SR-MM	All m_{CT} bins	low m_{CT}	med. m_{CT}	high m_{CT}
Observed	13	4	7	2
Expected	8.6 ± 2.2	4.6 ± 1.7	2.6 ± 1.3	1.4 ± 0.6
$t\bar{t}$	2.7 ± 1.4	1.6 ± 0.9	0.8 ± 0.7	0.30 ± 0.24
Single top	2.7 ± 1.9	1.6 ± 1.5	$1.0^{+1.1}_{-1.0}$	$0.15^{+0.19}_{-0.15}$
W+jets	1.5 ± 0.7	0.6 ± 0.4	$0.3^{+0.4}_{-0.3}$	0.57 ± 0.26
Di-/Multiboson	0.29 ± 0.08	0.09 ± 0.04	0.065 ± 0.028	0.14 ± 0.06
Others	1.33 ± 0.27	0.69 ± 0.20	0.40 ± 0.13	0.24 ± 0.09
SR-HM	All m_{CT} bins	low m_{CT}	med. m_{CT}	high m_{CT}
Observed	14	6	5	3
Expected	8.1 ± 2.7	4.1 ± 1.9	2.9 ± 1.3	1.1 ± 0.5
$t\bar{t}$	1.4 ± 0.5	0.8 ± 0.4	0.36 ± 0.25	0.22 ± 0.15
Single top	$2.0^{+2.4}_{-2.0}$	$0.9^{+1.5}_{-0.9}$	0.9 ± 0.9	$0.16^{+0.26}_{-0.16}$
W+jets	3.7 ± 1.0	1.9 ± 0.8	1.4 ± 0.8	0.45 ± 0.19
Di-/Multiboson	0.21 ± 0.06	0.057 ± 0.025	0.075 ± 0.027	0.08 ± 0.04
Others	0.74 ± 0.16	0.34 ± 0.09	0.19 ± 0.08	0.21 ± 0.08

8 Results

The observed event yields in each of the exclusion signal regions are summarized in Table 5 along with the corresponding standard model predictions obtained from the background-only fit. The background normalisation factors are $1.02^{+0.07}_{-0.09}$ for $t\bar{t}$, $0.6^{+0.5}_{-0.25}$ for single top, and $1.22^{+0.26}_{-0.24}$ for W+jets.

In Figure 2 the post-fit m_{CT} distributions in the $t\bar{t}$ control regions TR-LM, TR-MM and TR-HM are compared to the data. For the W and single top control regions the $m_{b\bar{b}}$ distribution is shown. Figure 3 shows the post-fit m_{CT} distributions after all of the validation region selection requirements applied other than the m_{CT} cut. Good agreement is observed between data and expectation in all validation regions (VR-onLM, VR-onMM, VR-onHM, VR-offLM, VR-offMM and VR-offHM).

The compatibility of the observed and expected event yields in control, validation, exclusion and discovery

Table 6: Left to right: 95% CL upper limits on the visible cross section ($\langle\epsilon\sigma\rangle^{95}_{\mathrm{obs}}$) and on the number of signal events (S^{95}_{obs}). The third column (S^{95}_{exp}) shows the expected 95% CL upper limit (and its $\pm 1\sigma$ excursions) of the number of signal events if no BSM signal is present. The last three columns indicate the $\mathrm{CL_B}$ value, i.e. the confidence level observed for the background-only hypothesis, the discovery p-value (p_0) and the significance Z.

Signal Region	$\langle\epsilon\sigma\rangle^{95}_{\mathrm{obs}}$[fb]	S^{95}_{obs}	S^{95}_{exp}	$\mathrm{CL_B}$	p_0	Z
SR-LM(disc.)	0.26	36.8	$20.0^{+8.0}_{-5.4}$	0.97	0.03	1.88
SR-MM(disc.)	0.18	24.8	$15.3^{+6.2}_{-4.6}$	0.94	0.06	1.54
SR-HM(disc.)	0.11	14.7	$9.7^{+3.3}_{-2.7}$	0.89	0.10	1.30

signal regions is illustrated in Figure 4. No significant excess is observed in data over the SM prediction. Figure 5 shows the post-fit m_{CT} distributions in SR-LM, SR-MM, and SR-HM. The uncertainty bands include all statistical and systematic uncertainties. The dashed lines represent the benchmark signal points.

Model-dependent exclusion limits at 95% CL are placed on the signal model. These limits are shown as a function of the masses of the supersymmetric particles in Figure 6. They are calculated using a likelihood similar to the one used in the background-only fit, but with additional terms for the SRs. The exclusion SRs thus participate in the fit and are used to constrain normalisation and nuisance parameters. A signal is allowed in this likelihood in both CRs and SRs. The VRs are not used in the fit. The $\mathrm{CL_s}$ method [75] is used to derive the confidence level of the exclusion for a particular signal model; signal models with a $\mathrm{CL_s}$ value below 0.05 are excluded at 95% CL. The uncertainties on the observed limit are calculated by varying the cross-section for the signal up and down by its uncertainty. Due to a modest excess observed in some bins of the exclusion signal regions, the observed limit is weaker than the expected and extends up to about 740 GeV in $m(\tilde{\chi}^{\pm}_1/\tilde{\chi}^0_2)$ for massless $\tilde{\chi}^0_1$ and up to approximately $m(\tilde{\chi}^{\pm}_1/\tilde{\chi}^0_2) = 600$ GeV for $m(\tilde{\chi}^0_1) = 250$ GeV. Benefiting from the increased luminosity and the improved two-dimensional fit procedure, the current observed limit extends the previous ATLAS limit by about 200 GeV in $m(\tilde{\chi}^{\pm}_1/\tilde{\chi}^0_2)$ for a massless $\tilde{\chi}^0_1$.

Table 6 summarizes the observed (S_{obs}) and expected (S_{exp}) 95% CL upper limits on the number of signal events and on the observed visible cross-section, $\langle\epsilon\sigma\rangle^{95}_{\mathrm{obs}}$, for each of the three cumulative discovery signal regions. These cumulative signal regions are those defined to test for the presence of any beyond-the-Standard-Model (BSM) physics processes, where in every case the upper criterion on m_{T} is also removed. Upper limits on contributions from new physics processes are estimated using the so-called "model-independent fit", where a generic BSM process is assumed to contribute only to the SR and not to the CRs, thus giving a conservative background estimate in the SR. When normalised to the integrated luminosity of the data sample, the results can be interpreted as corresponding to observed upper limits $\langle\epsilon\sigma\rangle^{95}_{\mathrm{obs}}$, defined as the product of the production cross-section, the acceptance and the selection efficiency of a BSM signal. The p_0 values, which represent the probability of the SM background alone to fluctuate to the observed number of events or higher, are also provided. All numbers are calculated based on pseudo-experiments.

9 Conclusion

A search for chargino-neutralino pairs decaying via an intermediate state of a Higgs boson and a W boson, into a final state with two b-tagged jets through the Higgs boson decay, a light lepton from the W boson
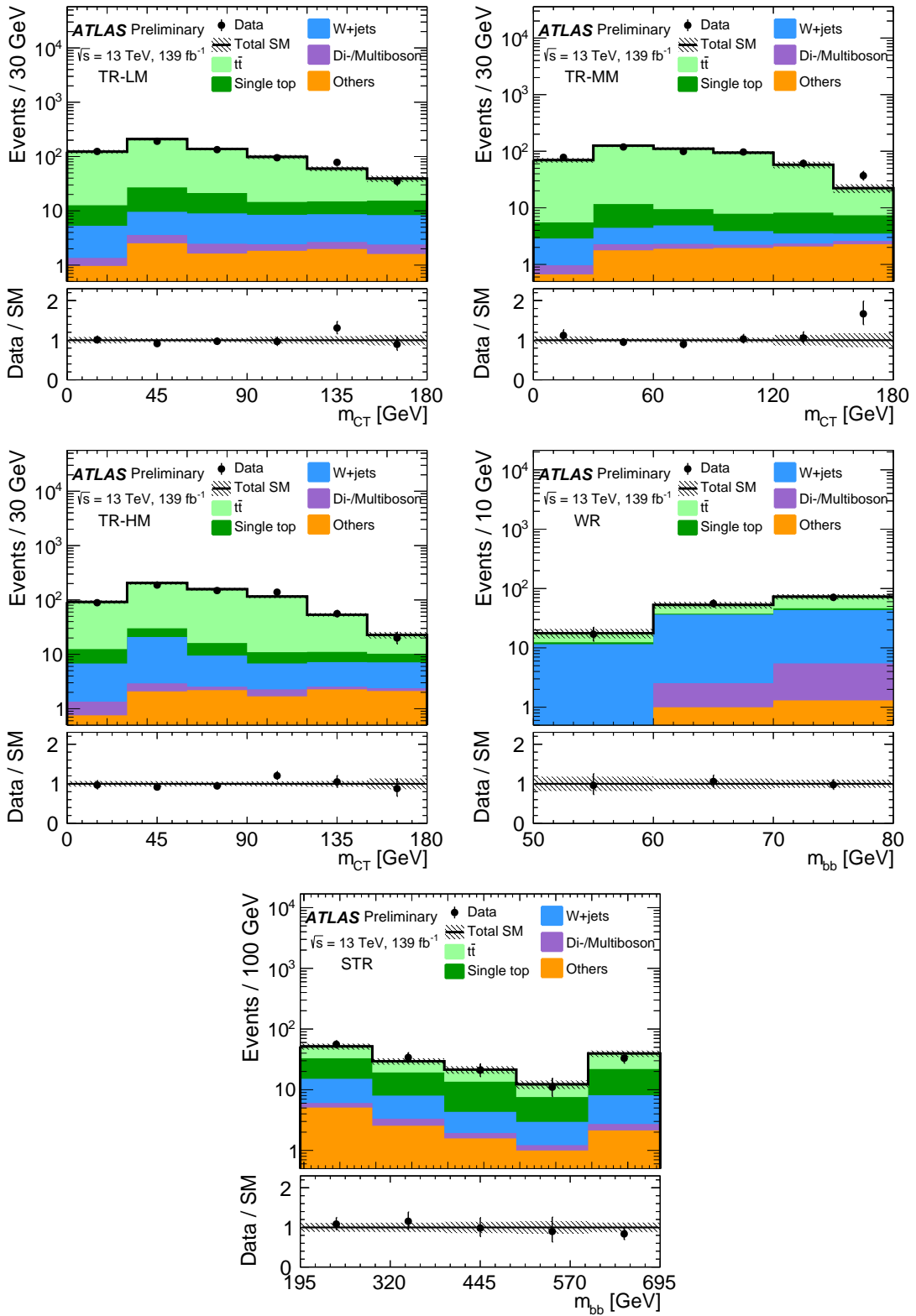
Figure 2: The post-fit m_{CT} distributions in TR-LM, TR-MM and TR-HM are shown as well as the post-fit $m_{b\bar{b}}$ distributions in WR and STR. The uncertainty bands plotted include all statistical and systematic uncertainties. The overflow events, where present, are included in the last bin.
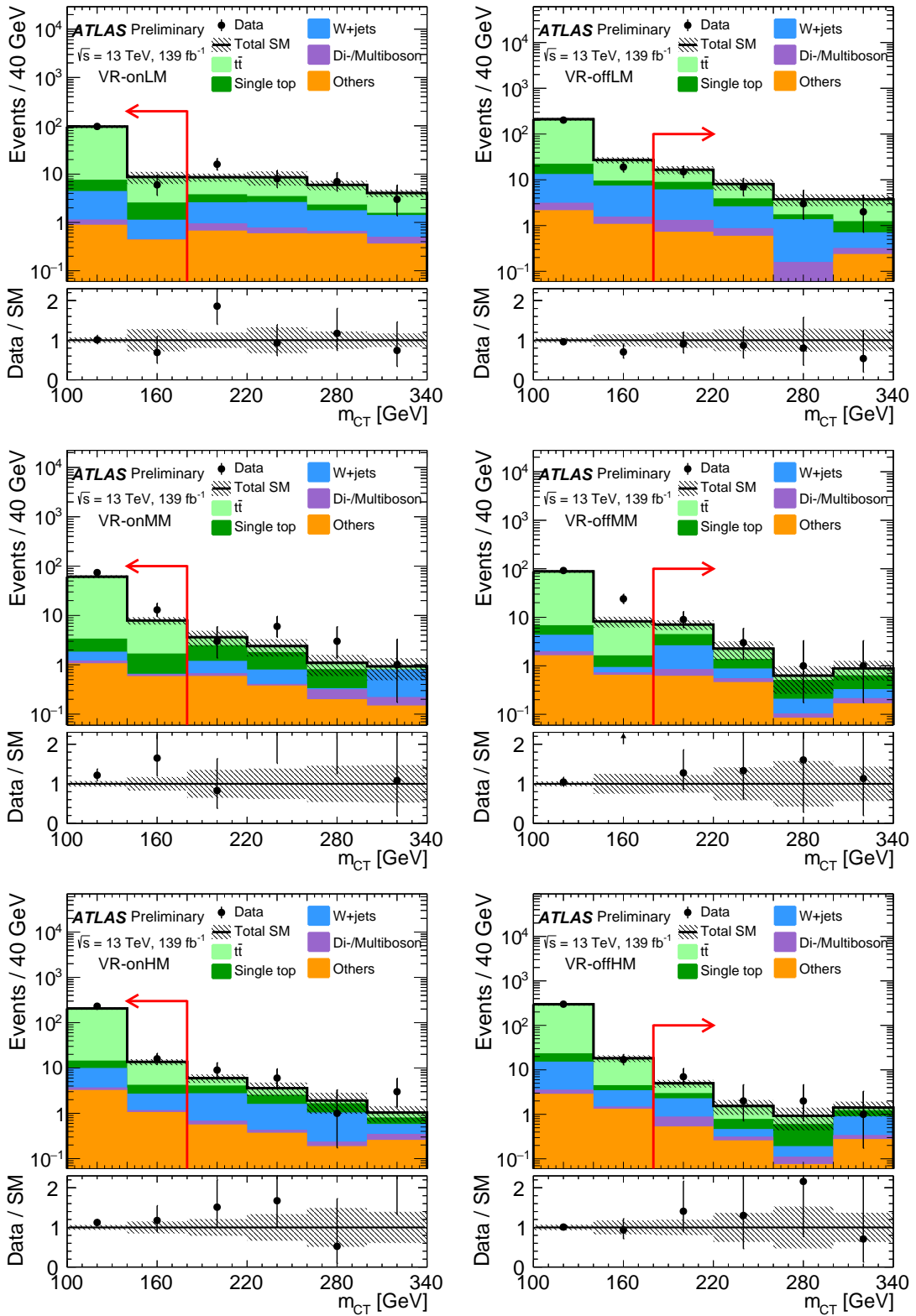
Figure 3: The post-fit m_{CT} distributions are shown in each of the validation regions (VR-onLM, VR-onMM, VR-onHM, VR-offLM, VR-offMM and VR-offHM) after all the selection requirements are applied other than the m_{CT} cut. The uncertainty bands plotted include all statistical and systematic uncertainties. The overflow (underflow) events, where present, are included in the last (first) bin. The red line with arrow indicates the m_{CT} cut used in VR selection.

14
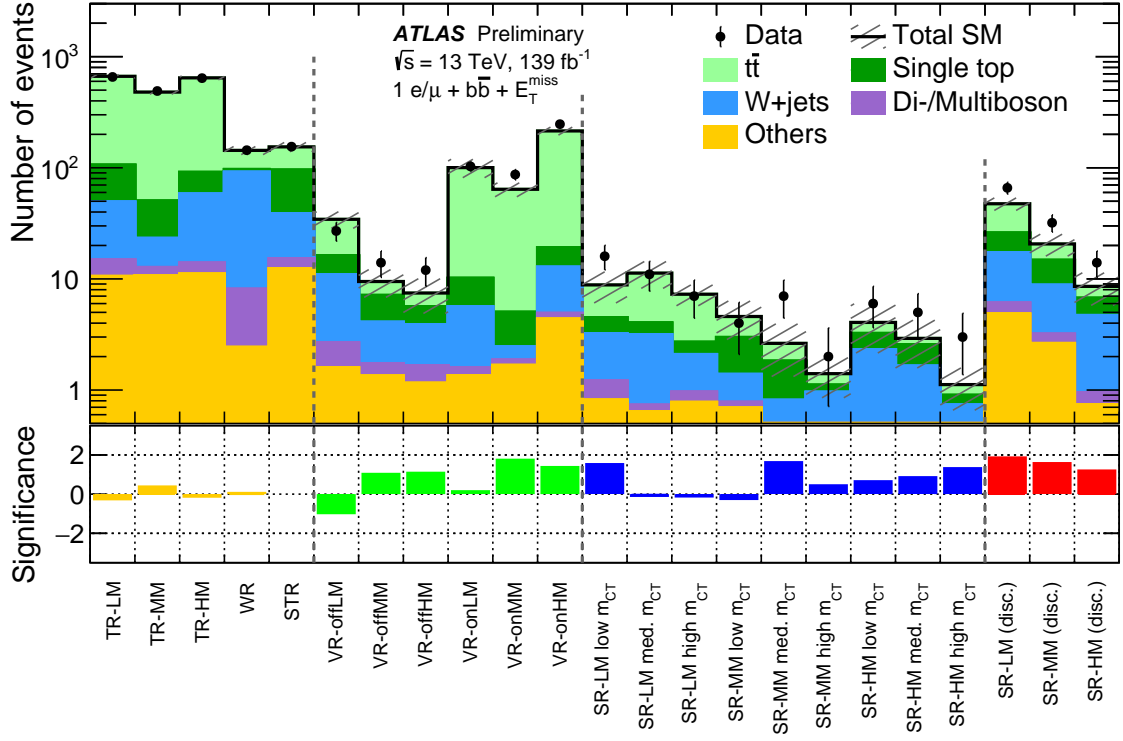
Figure 4: Comparison of the observed and expected event yields in control, validation, exclusion and discovery signal regions. Uncertainties in the background estimates include both the statistical (in the simulated event yields) and systematic uncertainties. The bottom panel shows the significance [74] of the differences between the observed and expected yields. Not all regions shown here are statistically independent.

decay and missing transverse momentum, is performed using pp collisions provided by the LHC at a centre-of-mass energy of 13 TeV. Data collected between 2015 and 2018 are used, corresponding to an integrated luminosity of 139 fb^{-1}. No significant deviation from the expected Standard Model background is observed. Limits are set on the direct production of the electroweakino in simplified models. The masses of $\tilde{\chi}_1^\pm / \tilde{\chi}_2^0$ up to 740 GeV are excluded at 95% confidence-level for a massless $\tilde{\chi}_1^0$. The sensitivity improves significantly the previous ATLAS limit by about 200 GeV in $m(\tilde{\chi}_1^\pm / \tilde{\chi}_2^0)$ for a massless $\tilde{\chi}_1^0$.
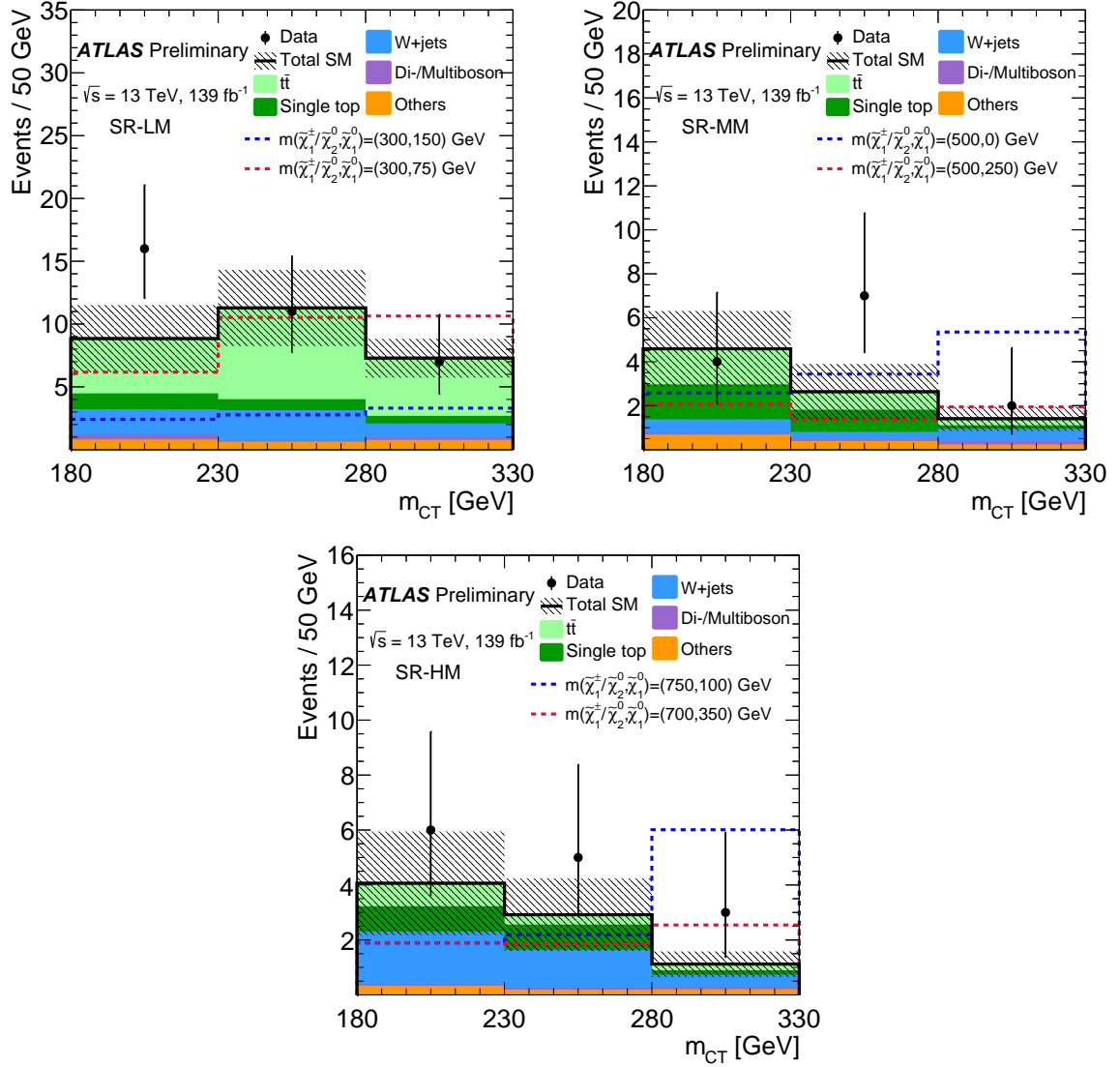
Figure 5: The post-fit m_{CT} distributions in the exclusion signal regions (SR-LM, SR-MM, and SR-HM). The uncertainty bands plotted include all statistical and systematic uncertainties. The dashed lines represent the benchmark signal samples. The overflow events, where present, are included in the last bin.
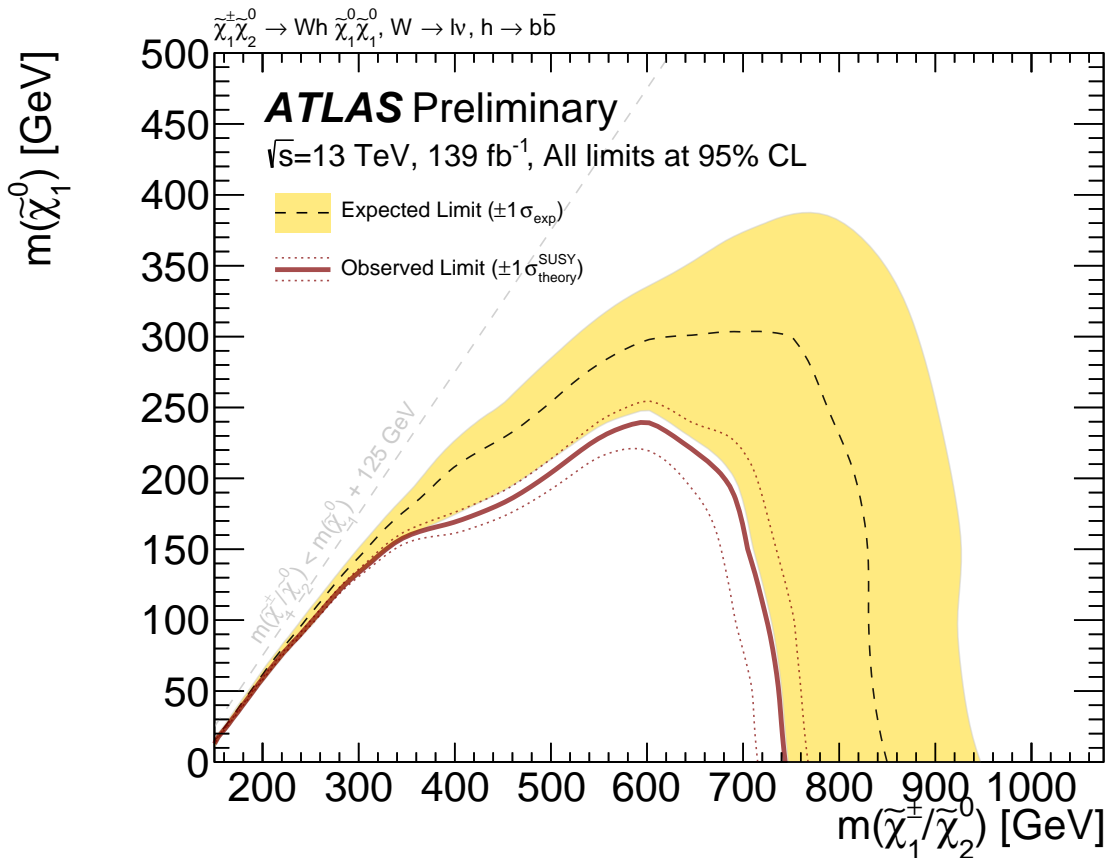
Figure 6: Model-dependent exclusion limits at 95 % CL on the production of a chargino and a next-to-lightest neutralino. The observed limit is given by the red solid line with the signal cross section uncertainties shown by the red dotted lines as indicated in the text. Expected limits are given by the black dashed line with uncertainties shown by the yellow band.

References

[1] ATLAS Collaboration, *Observation of a new particle in the search for the Standard Model Higgs boson with the ATLAS detector at the LHC*, Phys. Lett. B **716** (2012) 1, arXiv: `1207.7214 [hep-ex]`.

[2] CMS Collaboration, *Observation of a new boson at a mass of 125 GeV with the CMS experiment at the LHC*, Phys. Lett. B **716** (2012) 30, arXiv: `1207.7235 [hep-ex]`.

[3] ATLAS and CMS Collaborations, *Combined Measurement of the Higgs Boson Mass in pp Collisions at $\sqrt{s}$ = 7 and 8 TeV with the ATLAS and CMS Experiments*, Phys. Rev. Lett. **114** (2015) 191803, arXiv: `1503.07589 [hep-ex]`.

[4] ATLAS and CMS Collaborations, *Measurements of the Higgs boson production and decay rates and constraints on its couplings from a combined ATLAS and CMS analysis of the LHC pp collision data at $\sqrt{s}$ = 7 and 8 TeV*, JHEP **08** (2016) 045, arXiv: `1606.02266 [hep-ex]`.

[5] N. Sakai, *Naturalness in supersymmetric GUTS*, Z. Phys. C **11** (1981) 153.

[6] S. Dimopoulos, S. Raby and F. Wilczek, *Supersymmetry and the scale of unification*, Phys. Rev. D **24** (1981) 1681.

[7] L. E. Ibanez and G. G. Ross, *Low-energy predictions in supersymmetric grand unified theories*, Phys. Lett. B **105** (1981) 439.

[8] S. Dimopoulos and H. Georgi, *Softly broken supersymmetry and SU(5)*, Nucl. Phys. B **193** (1981) 150.

[9] Y. A. Golfand and E. P. Likhtman, *Extension of the Algebra of Poincare Group Generators and Violation of P invariance*, JETP Lett. **13** (1971) 323, [Pisma Zh. Eksp. Teor. Fiz. **13** (1971) 452].

[10] D. V. Volkov and V. P. Akulov, *Is the neutrino a goldstone particle?*, Phys. Lett. B **46** (1973) 109.

[11] J. Wess and B. Zumino, *Supergauge transformations in four-dimensions*, Nucl. Phys. B **70** (1974) 39.

[12] J. Wess and B. Zumino, *Supergauge invariant extension of quantum electrodynamics*, Nucl. Phys. B **78** (1974) 1.

[13] S. Ferrara and B. Zumino, *Supergauge invariant Yang-Mills theories*, Nucl. Phys. B **79** (1974) 413.

[14] A. Salam and J. A. Strathdee, *Super-symmetry and non-Abelian gauges*, Phys. Lett. B **51** (1974) 353.

[15] G. R. Farrar and P. Fayet, *Phenomenology of the production, decay, and detection of new hadronic states associated with supersymmetry*, Phys. Lett. B **76** (1978) 575.

[16] H. Goldberg, *Constraint on the Photino Mass from Cosmology*, Phys. Rev. Lett. **50** (1983) 1419, [Erratum: Phys. Rev. Lett. **103** (2009) 099905].

[17] J. R. Ellis, J. S. Hagelin, D. V. Nanopoulos, K. A. Olive and M. Srednicki, *Supersymmetric relics from the big bang*, Nucl. Phys. B **238** (1984) 453.

[18] R. Barbieri and G. F. Giudice, *Upper bounds on supersymmetric particle masses*, Nucl. Phys. B **306** (1988) 63.

[19] B. de Carlos and J. A. Casas, *One loop analysis of the electroweak breaking in supersymmetric models and the fine tuning problem*, Phys. Lett. B **309** (1993) 320, arXiv: `hep-ph/9303291 [hep-ph]`.

[20] P. Fayet, *Supersymmetry and Weak, Electromagnetic and Strong Interactions*, Phys. Lett. B **64** (1976) 159.

[21] P. Fayet, *Spontaneously broken supersymmetric theories of weak, electromagnetic and strong interactions*, Phys. Lett. B **69** (1977) 489.

[22] J. Gunion et al., *Calculation and Phenomenology of Two Body Decays of Neutralinos and Charginos to W, Z, and Higgs Bosons*, Int. J. Mod. Phys. A **2** (1987) 1145.

[23] T. Moroi, *Muon anomalous magnetic dipole moment in the minimal supersymmetric standard model*, Phys. Rev. D **53** (11 1996) 6565, URL: https://doi.org/10.1103/PhysRevD.53.6565.

[24] T. Moroi, *Erratum: Muon anomalous magnetic dipole moment in the minimal supersymmetric standard model [Phys. Rev. D 53, 6565 (1996)]*, Phys. Rev. D **56** (7 1997) 4424, URL: https://link.aps.org/doi/10.1103/PhysRevD.56.4424.

[25] J. L. Feng and T. Moroi, *Supernatural supersymmetry: Phenomenological implications of anomaly-mediated supersymmetry breaking*, Phys. Rev. D **61** (9 2000) 095004, URL: https://link.aps.org/doi/10.1103/PhysRevD.61.095004.

[26] ATLAS Collaboration, *Search for chargino and neutralino production in final states with a Higgs boson and missing transverse momentum at $\sqrt{s}$ = 13 TeV with the ATLAS detector*, Phys. Rev. D (2018), arXiv: 1812.09432 [hep-ex].

[27] ATLAS Collaboration, *Search for direct production of electroweakinos in final states with missing transverse energy and a Higgs boson decaying into photons in pp collisions at $\sqrt{s}$ = 13 TeV with the ATLAS detector*, ATLAS-CONF-2019-019, 2019, URL: https://cds.cern.ch/record/2676596.

[28] CMS Collaboration, *Combined search for electroweak production of charginos and neutralinos in proton-proton collisions at $\sqrt{s}$ = 13 TeV*, JHEP **03** (2018) 160, arXiv: 1801.03957 [hep-ex].

[29] ATLAS Collaboration, *The ATLAS Experiment at the CERN Large Hadron Collider*, JINST **3** (2008) S08003.

[30] ATLAS Collaboration, *ATLAS Insertable B-Layer Technical Design Report*, ATLAS-TDR-19, 2010, URL: https://cds.cern.ch/record/1291633, *ATLAS Insertable B-Layer Technical Design Report Addendum*, ATLAS-TDR-19-ADD-1, 2012, URL: https://cds.cern.ch/record/1451888.

[31] ATLAS IBL Collaboration, *Production and integration of the ATLAS Insertable B-Layer*, JINST **13** (2018) T05008, arXiv: 1803.00844 [physics.ins-det].

[32] ATLAS Collaboration, *Luminosity determination in pp collisions at $\sqrt{s}$ = 8 TeV using the ATLAS detector at the LHC*, Eur. Phys. J. C **76** (2016) 653, arXiv: 1608.03953 [hep-ex].

[33] G. Avoni et al., *The new LUCID-2 detector for luminosity measurement and monitoring in ATLAS*, JINST **13** (2018) P07017.

[34] ATLAS Collaboration, *The ATLAS Simulation Infrastructure*, Eur. Phys. J. C **70** (2010) 823, arXiv: 1005.4568 [physics.ins-det].

[35] S. Agostinelli et al., *GEANT4 - a simulation toolkit*, Nucl. Instrum. Meth. A **506** (2003) 250.

[36] D. J. Lange, *The EvtGen particle decay simulation package*, Nucl. Instrum. Meth. A **462** (2001) 152.

[37] L. Lönnblad and S. Prestel, *Merging multi-leg NLO matrix elements with parton showers*, JHEP **03** (2013) 166, arXiv: 1211.7278 [hep-ph].

[38] J. Alwall et al., *The automated computation of tree-level and next-to-leading order differential cross sections, and their matching to parton shower simulations*, JHEP **07** (2014) 079, arXiv: 1405.0301 [hep-ph].

[39] T. Sjöstrand, S. Mrenna and P. Z. Skands, *A brief introduction to PYTHIA 8.1*, Comput. Phys. Commun. **178** (2008) 852, arXiv: 0710.3820 [hep-ph].

[40] ATLAS Collaboration, *ATLAS Pythia 8 tunes to* 7 *TeV data*, ATL-PHYS-PUB-2014-021, 2014, URL: https://cds.cern.ch/record/1966419.

[41] R. D. Ball et al., *Parton distributions with LHC data*, Nucl. Phys. B **867** (2013) 244, arXiv: 1207.1303 [hep-ph].

[42] W. Beenakker, M. Kramer, T. Plehn, M. Spira and P. M. Zerwas, *Stop production at hadron colliders*, Nucl. Phys. B **515** (1998) 3, arXiv: hep-ph/9710451 [hep-ph].

[43] W. Beenakker et al., *Supersymmetric top and bottom squark production at hadron colliders*, JHEP **08** (2010) 098, arXiv: 1006.4771 [hep-ph].

[44] W. Beenakker et al., *Squark and Gluino Hadroproduction*, Int. J. Mod. Phys. A **26** (2011) 2637, arXiv: 1105.1110 [hep-ph].

[45] C. Borschensky et al., *Squark and gluino production cross sections in pp collisions at* $\sqrt{s}$ = *13, 14, 33 and 100 TeV*, Eur. Phys. J. C **74** (2014) 3174, arXiv: 1407.5066 [hep-ph].

[46] S. Alioli, P. Nason, C. Oleari and E. Re, *A general framework for implementing NLO calculations in shower Monte Carlo programs: the POWHEG BOX*, JHEP **06** (2010) 043, arXiv: 1002.2581 [hep-ph].

[47] S. Frixione, P. Nason and C. Oleari, *Matching NLO QCD computations with parton shower simulations: the POWHEG method*, JHEP **11** (2007) 070, arXiv: 0709.2092 [hep-ph].

[48] M. Czakon and A. Mitov, *Top++: A program for the calculation of the top-pair cross-section at hadron colliders*, Comput. Phys. Commun. **185** (2014) 2930, arXiv: 1112.5675 [hep-ph].

[49] LHCTopWG, *NLO single-top channel cross sections*, (2017), URL: https://twiki.cern.ch/twiki/bin/view/LHCPhysics/SingleTopRefXsec.

[50] T. Gleisberg et al., *Event generation with SHERPA 1.1*, JHEP **02** (2009) 007, arXiv: 0811.4622 [hep-ph].

[51] C. Anastasiou, L. J. Dixon, K. Melnikov and F. Petriello, *High precision QCD at hadron colliders: Electroweak gauge boson rapidity distributions at NNLO*, Phys. Rev. D **69** (2004) 094008, arXiv: hep-ph/0312266.

[52] P. Bärnreuther, M. Czakon and A. Mitov, *Percent Level Precision Physics at the Tevatron: First Genuine NNLO QCD Corrections to* $q\bar{q} \to t\bar{t} + X$, Phys. Rev. Lett. **109** (2012) 132001, arXiv: 1204.5201 [hep-ph].

[53] ATLAS Collaboration, *Measurement of the* Z/γ^* *boson transverse momentum distribution in pp collisions at* $\sqrt{s}$ = 7 *TeV with the ATLAS detector*, JHEP **09** (2014) 145, arXiv: 1406.3660 [hep-ex].

[54] P. M. Nadolsky et al., *Implications of CTEQ global analysis for collider observables*, Phys. Rev. D **78** (2008) 013004, arXiv: 0802.0007 [hep-ph].

[55] D. de Florian et al., *Handbook of LHC Higgs cross sections: 4. Deciphering the nature of the Higgs sector*, CERN-2017-002-M (2016), arXiv: 1610.07922 [hep-ph].

[56] ATLAS Collaboration, *Vertex Reconstruction Performance of the ATLAS Detector at* $\sqrt{s}$ = 13 *TeV*, ATL-PHYS-PUB-2015-026, 2015, URL: https://cds.cern.ch/record/2037717.

[57] ATLAS Collaboration, *Selection of jets produced in* 13 *TeV proton–proton collisions with the ATLAS detector*, ATLAS-CONF-2015-029, 2015, URL: https://cds.cern.ch/record/2037702.

[58] ATLAS Collaboration, *Electron reconstruction and identification in the ATLAS experiment using the 2015 and 2016 LHC proton–proton collision data at* $\sqrt{s} = 13\,TeV$, CERN-EP-2018-273 (2019), arXiv: 1902.04655 [hep-ex].

[59] ATLAS Collaboration, *Electron efficiency measurements with the ATLAS detector using the 2015 LHC proton–proton collision data*, ATLAS-CONF-2016-024, 2016, URL: https://cds.cern.ch/record/2157687.

[60] ATLAS Collaboration, *Muon reconstruction performance of the ATLAS detector in proton–proton collision data at* $\sqrt{s} = 13\,TeV$, Eur. Phys. J. C **76** (2016) 292, arXiv: 1603.05598 [hep-ex].

[61] M. Cacciari, G. P. Salam and G. Soyez, *The anti-k_t jet clustering algorithm*, JHEP **04** (2008) 063, arXiv: 0802.1189 [hep-ph].

[62] ATLAS Collaboration, *Performance of pile-up mitigation techniques for jets in pp collisions at* $\sqrt{s} = 8\,TeV$ *using the ATLAS detector*, Eur. Phys. J. C **76** (2016) 581, arXiv: 1510.03823 [hep-ex].

[63] ATLAS Collaboration, *Measurements of b-jet tagging efficiency with the ATLAS detector using* $t\bar{t}$ *events at* $\sqrt{s} = 13\,TeV$, JHEP **08** (2018) 089, arXiv: 1805.01845 [hep-ex].

[64] ATLAS Collaboration, *Optimisation of the ATLAS b-tagging performance for the 2016 LHC Run*, ATL-PHYS-PUB-2016-012, 2016, URL: https://cds.cern.ch/record/2160731.

[65] M. Cacciari, G. P. Salam and G. Soyez, *The catchment area of jets*, JHEP **04** (2008) 005, arXiv: 0802.1188 [hep-ph].

[66] ATLAS Collaboration, *Measurement of the photon identification efficiencies with the ATLAS detector using LHC Run 2 data collected in 2015 and 2016*, Eur. Phys. J. C **79** (2019) 205, arXiv: 1810.05087 [hep-ex].

[67] ATLAS Collaboration, *Performance of missing transverse momentum reconstruction with the ATLAS detector using proton–proton collisions at* $\sqrt{s} = 13\,TeV$, Eur. Phys. J. C **78** (2018) 903, arXiv: 1802.08168 [hep-ex].

[68] ATLAS Collaboration, E_T^{miss} *performance in the ATLAS detector using 2015–2016 LHC pp collisions*, ATLAS-CONF-2018-023, 2018, URL: https://cds.cern.ch/record/2625233.

[69] D. R. Tovey, *On measuring the masses of pair-produced semi-invisibly decaying particles at hadron colliders*, JHEP **04** (2008) 034, arXiv: 0802.2879 [hep-ph].

[70] G. Polesello and D. R. Tovey, *Supersymmetric particle mass measurement with the boost-corrected contransverse mass*, JHEP **03** (2010) 030, arXiv: 0910.0174 [hep-ph].

[71] ATLAS Collaboration, *Simulation of top-quark production for the ATLAS experiment at* $\sqrt{s} = 13\,TeV$, ATL-PHYS-PUB-2016-004, 2016, URL: https://cds.cern.ch/record/2120417.

[72] ATLAS Collaboration, *Multi-boson simulation for* 13 *TeV ATLAS analyses*, ATL-PHYS-PUB-2016-002, 2016, URL: https://cds.cern.ch/record/2119986.

[73] ATLAS Collaboration, *Jet energy scale measurements and their systematic uncertainties in proton–proton collisions at* $\sqrt{s} = 13\,TeV$ *with the ATLAS detector*, Phys. Rev. D **96** (2017) 072002, arXiv: 1703.09665 [hep-ex].

[74] R. D. Cousins, J. T. Linnemann and J. Tucker, *Evaluation of three methods for calculating statistical significance when incorporating a systematic uncertainty into a test of the background-only hypothesis for a Poisson process*, Nucl. Instrum. Meth. A **595** (2008) 480, arXiv: physics/0702156 [physics.data-an].

[75] A. L. Read, *Presentation of search results: The CL_S technique*, J. Phys. G **28** (2002) 2693.

Appendix
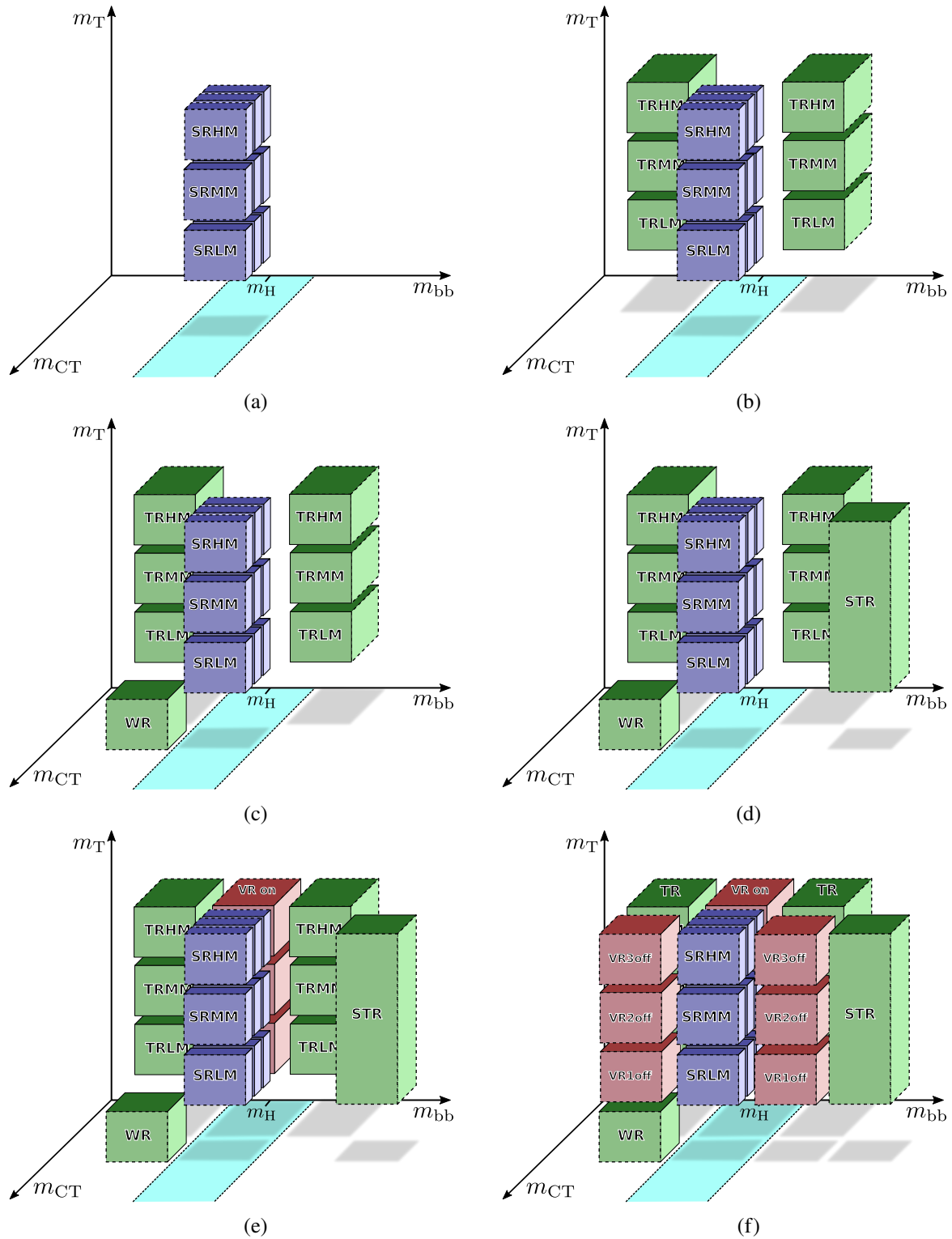
Figure 7: Illustration of all regions of interest used in the analysis.
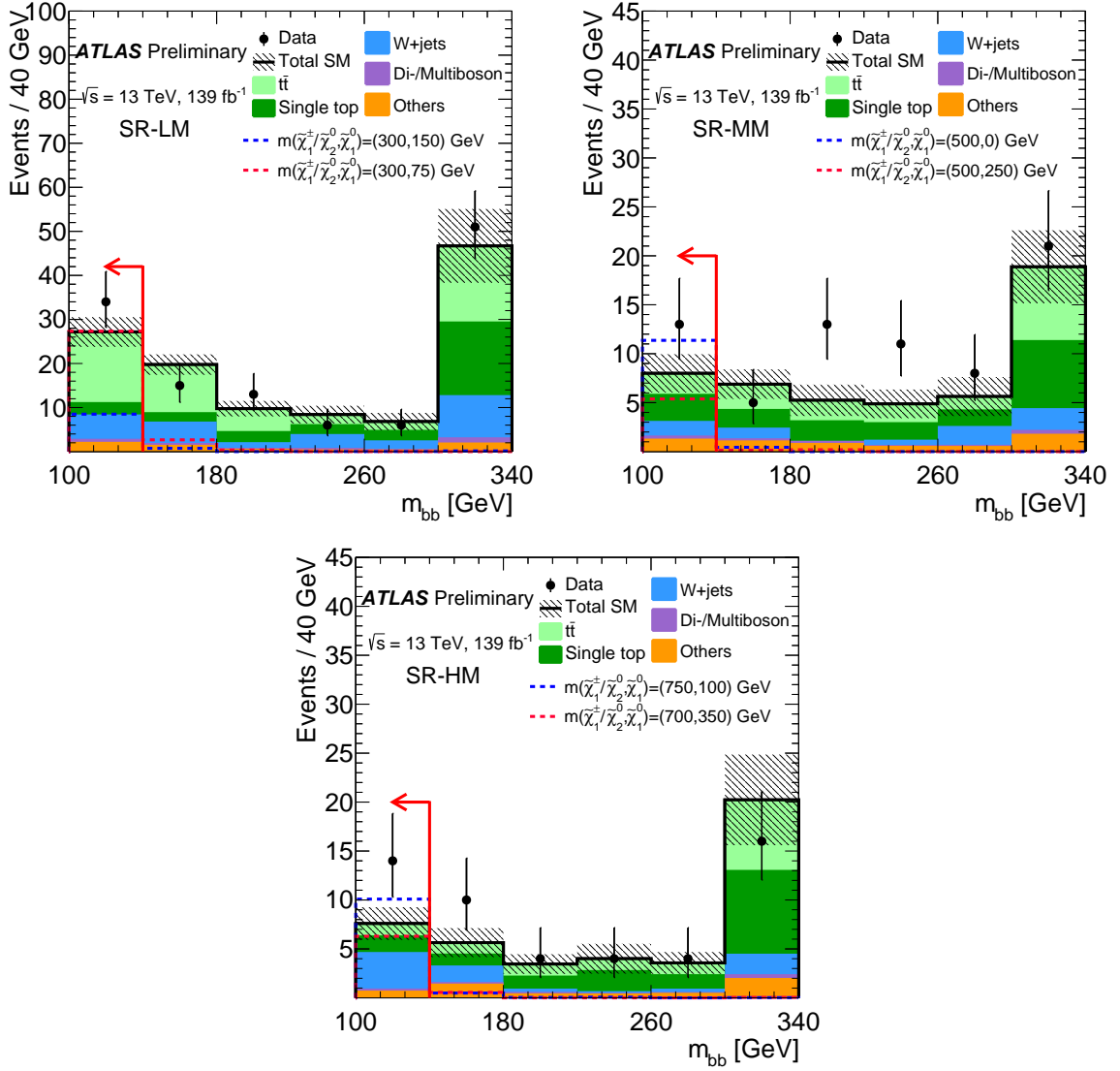
Figure 8: The post-fit $m_{b\bar{b}}$ distributions after all of the signal region (SR-LM, SR-MM, and SR-HM) selection requirements applied other than the $m_{b\bar{b}}$ cut. The uncertainty bands plotted include all statistical and systematic uncertainties. The dashed lines represent the benchmark signal samples. The overflow events, where present, are included in the last bin. The red line with arrow indicates the $m_{b\bar{b}}$ cut used in SR selection.